

Colloidal Silver Nanoparticle Plasmonic Arrays for Versatile Lasing Architectures via Template-Assisted Self-Assembly

Ylli Conti, Nicolas Passarelli, Jose Mendoza-Carreño, Leonardo Scarabelli,*
and Agustin Mihi*

The characteristic narrow spectral features of surface lattice resonances emerge as great candidates for the rational design of optical nanocavities targeting enhanced light-matter interaction, ultrasensitive detection, or efficient light-energy conversion. Traditional fabrication of metal arrays involves thermal evaporation and annealing steps, limiting scalability and adaptability. In contrast, template-assisted self-assembly provides a high-throughput all-around approach for implementing colloidal plasmonic metasurfaces on a variety of different materials. Here, the use of pre-synthesized silver nanoparticles is designed and tested for the construction of versatile lasing architectures. Plasmonic arrays are prepared directly on top of the gain media (a photoresist thin film doped with Rhodamine B), creating optical nanocavities with quality factors as high as 85. The proposed architecture circumvents the need for an index-matching superstrate to promote the generation of collective resonances, leaving the plasmonic surface accessible for post-assembly modification. Additionally, the angular dispersion of the metasurfaces is used to modify the angle of the lasing emission, achieving both normal and off-normal lasing upon modification of the lattice parameter of the array. The results demonstrate how state-of-the-art colloidal self-assembly techniques offer a scalable and versatile alternative for the fabrication of plasmonic and photonic devices targeting advanced and non-linear optical phenomena.


1. Introduction

Metal nanoparticles (NPs) can sustain strong collective oscillations of their conduction electrons, known as localized surface plasmon resonances, with energies falling in the visible and infrared (IR) regions of the electromagnetic spectrum.^[1] The plasmon resonance frequency can be tuned by modifying the particle size, shape, composition, and local dielectric environment.^[2–4] Additionally, plasmonic metal NPs can serve as building blocks for the manufacturing of photonic structures such as ordered arrays, where the localized plasmons can undergo long-range coupling and hybridize with diffractive states satisfying Bragg scattering conditions, i.e., Rayleigh-Wood anomalies (R-W).^[5] The result of this hybridization is the emergence of surface lattice plasmon resonances (SLRs), which can be spectrally tuned from the ultraviolet (UV) to the IR varying the lattice parameter of the array (Λ), the refractive index of the surrounding medium, and the illumination angle.^[6] Under these circumstances, the light scattered by each plasmonic unit in the plane of the array at

the R-W position will be in phase,^[6] sustaining a standing wave instead of decaying into free space. Hence, the plasmonic resonance is reinforced by the diffractive coupling, and the optical losses are partially mitigated due to the periodic configuration. Plasmonic arrays preserve the properties of the individual components, such as an enhanced scattering cross-section, typical of plasmonic resonances, while displaying at the same time narrow bandwidths, high-quality factors^[7] (Q -factors, a resonance figure of merit defined as $\omega/\Delta\omega$), and spatial delocalization typical of diffractive phenomena.^[8] Because of these properties, SLRs can be exploited to promote non-linear optical phenomena such as surface enhanced Raman effects^[9–11] and lasing.^[12–18]

The fabrication of plasmonic arrays with sub-wavelength dimensions requires advanced nanofabrication techniques,^[19] including extreme UV lithography, focused ion beam, and electron beam lithography and evaporation. These approaches can access nanometric features, but their implementation for low-cost mass production remains a challenge. To overcome these limitations, phase shift photolithography, etching, electron-beam deposition, and lift-off steps were combined in a process known

Y. Conti, N. Passarelli^[+], J. Mendoza-Carreño, L. Scarabelli, A. Mihi
Institute of Materials Science of Barcelona (ICMAB-CSIC)
Campus de la UAB
Bellaterra 08193, Spain
E-mail: lscarabelli@icmab.es; amihi@icmab.es

 The ORCID identification number(s) for the author(s) of this article can be found under <https://doi.org/10.1002/adom.202300983>

^[+]Present address: School of Mathematical and Physical Sciences, University of Technology Sydney, Building 4/745 Harris St, Ultimo, NSW 2007, Sydney 08193, Australia

© 2023 The Authors. Advanced Optical Materials published by Wiley-VCH GmbH. This is an open access article under the terms of the Creative Commons Attribution-NonCommercial-NoDerivs License, which permits use and distribution in any medium, provided the original work is properly cited, the use is non-commercial and no modifications or adaptations are made.

DOI: 10.1002/adom.202300983

as *PEEL*, which exploits a physical deposition mask to fabricate high-quality plasmonic arrays on-demand with a misalignment of less than 5° .^[20] This technology has been extensively involved in the preparation of plasmonic-based lasing architectures, where a gain medium is applied on top of the pre-fabricated plasmonic cavity.^[21] The development of plasmonic nanolaser architectures enables low threshold emission, real-time wavelength tunability,^[14,22] and off-normal^[23] and azimuthal polarized^[24] emission.

An exciting alternative for the large-scale preparation of plasmonic substrates is represented by the colloidal self-assembly of pre-synthesized plasmonic NPs.^[9,25–31] Metal colloids have the advantage of scalable production and high crystallinity, avoiding metal deposition by thermal evaporation or sputtering processes. Moreover, the use of colloidal building blocks offers the possibility of controlling the surface chemistry of the environment, targeting responsive dynamic functionalities. Amongst the different colloidal self-assembly approaches, template-assisted self-assembly enforces colloidal organization at the nanoscale through the confinement of a concentrated NP suspension under a patterned elastomeric stamp, leaving the solvent to evaporate over the course of a few hours. During solvent evaporation, Van der Waals interactions between the NPs and capillary forces within the cavities of the template drive the organization of the colloids into close-packed nanostructures exhibiting *fcc* or *hcp* crystal lattices.^[32–34] Self-organization begins when the thickness of the solvent layer becomes approximately equal to the particle diameter,^[32,35] with solvent evaporation rate, and NP shape and surface chemistry determining the quality of the obtained assemblies.^[33] Additionally, fluid dynamic phenomena such as the Marangoni and the coffee ring effects can significantly alter the assembly's large-scale uniformity.^[36,37] The availability of such a variety of different control handles is what makes template-assisted self-assembly extremely versatile and compatible with different colloids, solvents, and surfaces. Recent advances in template-assisted colloidal self-assembly of gold NPs led to the demonstration of SLRs with *Q*-factors above 60,^[38–40] with the reduction of radiative damping resulting in an increase of the mode quality.^[41] These results suggest that template-assisted self-assembly is now a suitable approach for the fabrication of high-quality optical cavities, targeting advanced light applications such as lasing, strong coupling, or second harmonic generation.

In this work, we fabricate SLR-based lasing architectures through the self-assembly of pre-synthesized silver colloids. The plasmonic optical cavity is manufactured directly on top of a photoresist layer containing Rhodamine B (RhB) that will serve as optical gain media,^[42] readily producing high *Q*-factor resonances without the need for further processing or annealing, compared to standard top-down lithography. In this context, the high throughput and versatility of colloidal self-assembly facilitates the study of different NP geometries and materials,^[43–47] and enables the exploration of dynamic control of the chemical and physical interactions at the interface between the plasmonic/photonic structures and the gain media underneath, as well as at the exposed surface of the assembly. The prepared architectures were capable of inducing population inversion in the gain media. The consequent lasing emission was fully characterized with a customized optical setup with excellent agreement

with theoretical simulations. Moreover, we test the versatility of our fabrication scheme, targeting off-normal lasing emission by modifying the geometry of the plasmonic array.

2. Results and Discussion

2.1. Preparation of the Lasing Architecture

Silver nanoparticles (AgNPs) with an average diameter of 23 ± 3 nm were organized into square arrays with lattice parameters (Λ) of 400, 500, and 600 nm using pre-patterned polydimethylsiloxane (PDMS) molds as templates (see Table S1 and Figure S1, Supporting Information). Silver was chosen as plasmonic material (instead of gold or copper) due to the specific characteristics of its dielectric function which translates in reduced optical losses and greater plasmonic performances in the visible part of the electromagnetic spectra.^[48] Moreover, the NP size was selected to guarantee a high scattering field, promoting far-field coupling within the plasmonic array, while limiting at the same time near-field interactions.^[39] It is important to highlight how the use of bigger nanoparticles would imply a significant redshift and broadening effect of the plasmonic response, which would increase optical losses,^[49] as exemplified in Figure S5 (Supporting Information) for 50 nm Ag colloids.^[39] The AgNPs were finally coated with poly(ethylene glycol) methyl ether thiol (PEG) with an average molecular weight of 2000 g mol^{-1} to ensure their long-term colloidal stability and resistance toward oxidation.^[50]

The lasing architectures were prepared in a single fabrication step. By taking advantage of the versatility and adaptability of template-assisted self-assembly, silver plasmonic arrays were assembled directly on top of the active gain media of choice (Figure 1). Specifically, Rhodamine B (RhB) was dissolved into a diluted solution of SU8 2000.5 photoresist (7% w/w, Microchem) and subsequently spin coated onto a glass slide (see Experimental Section). This procedure leads to an active layer with a thickness of 250 nm (confirmed by both profilometry and interferometry measurements, Figure S2, Supporting Information), and a final RhB concentration of 2.8% w/w (assuming complete evaporation of the thinner).^[51] The SU8 monomer is activated during UV light exposure, and the polymerization is carried out in the following hard bake step, which also controls the porosity of the final layer.^[52] After the preparation of the active media thin films, a large scale ($\approx 0.5 \text{ cm}^2$) and uniform assembly is achieved using a concentrated AgNPs colloidal suspension in a water:ethanol (6:4) mixture in the presence of $50 \mu\text{M}$ cetyltrimethylammonium chloride (CTAC, Figure 1A–C). Moreover, the extinction spectra of the AgNPs suspension were used to optimize the concentration of the colloid deposited on the surface, ensuring sample-to-sample reproducibility (Figure S10, Supporting Information). A more general discussion over the effect of solvent composition and surfactant concentration was reported in the previous publications by our and other groups.^[9,38,53]

The high large-scale quality of the prepared plasmonic arrays is confirmed by scanning electron microscopy (SEM) analysis (Figure 1D). Compare to the results obtained on simple glass substrates, the hydrophobicity of the SU8 layer seems to improve the self-assembly process.^[36,37,54] We hypothesize that the hydrophobic environment induces dewetting within the stamp

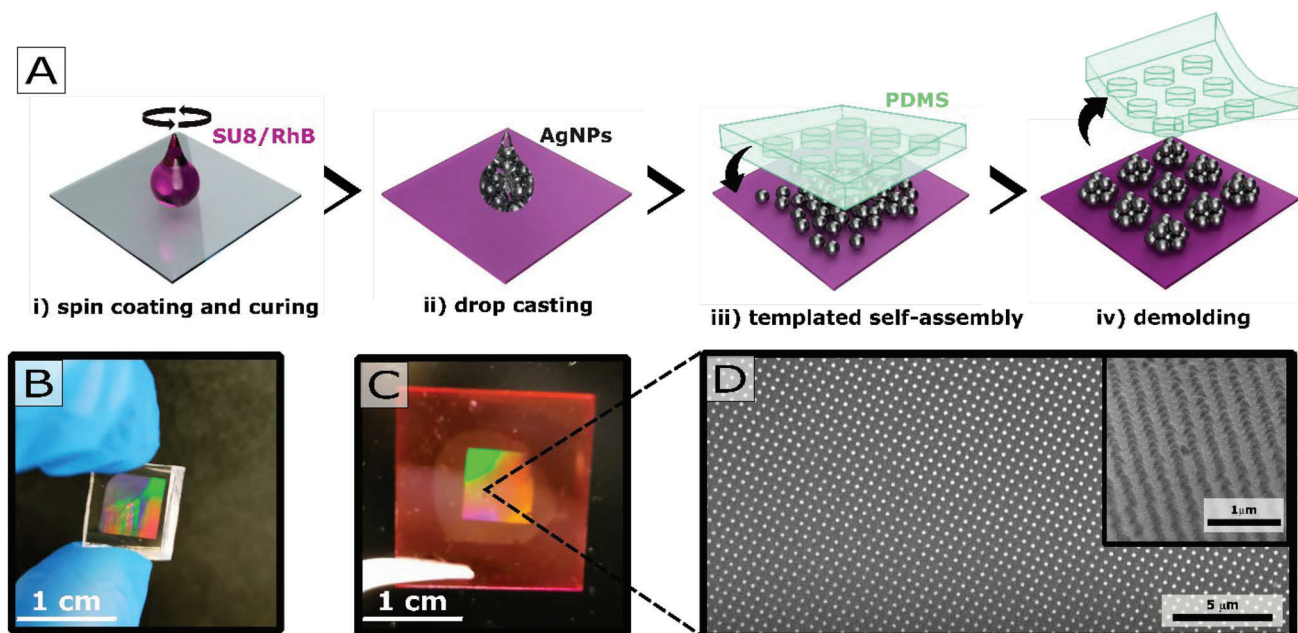


Figure 1. Fabrication of the lasing architectures. A) Schematic representation of the fabrication steps. From left to right: i) spin-coating of the SU8-dye mixture and curing, ii) drop casting of the nanoparticle suspension, iii) application of the polydimethylsiloxane (PDMS) stamp and template-assisted self-assembly, and iv) demolding of the PDMS stamp after complete drying (all the details of the procedure can be found in the experimental section in the Supporting Information). B,C) Pictures of the PDMS stamp (B), and of the final sample (C). D) Low magnification scanning electron microscopy images of a silver plasmonic colloidal array taken in top-view (D) and at 45° inclination (inset), showing the high uniformity of the fabricated structures.

nanocavities, achieving a higher fidelity in the reproduction of the stamp geometry (Figure S11, Supporting Information).^[55,56]

2.2. Optical and Structural Characterization of the Plasmonic Cavity

The thickness of the spin-coated SU8-RhB gain media layer plays a central role in the optical properties of the system. In fact, the refractive index mismatch between the substrate (glass) and superstrate (air) can generate wave-guiding effects.^[51] In our experiments, the thickness of the SU8-RhB layer was selected to be sufficiently thin in order to sustain a single-waveguide mode, while ensuring at the same time a phase match to favor the coupling between the plasmonic grating and the gain media.^[51,57] Under these conditions, the resulting 250 nm thick photoresist film (Figure S2, Supporting Information) is expected to favor the hybridization between the sustained waveguided modes and the collective SLRs of the silver plasmonic array. This interaction enables the formation of hybrid waveguide-SLR modes that increase the out-coupling efficiency of the system with the far field, which translates into an even narrower peak bandwidth.^[16,23,24,58–60] Along the normal direction, the spectral position of the Rayleigh-Wood (R-W) anomalies of the square lattice can be described as $\lambda = \frac{\lambda_{x,y}}{\sqrt{(m^2 + l^2)}} \cdot n_{eff}$, where m and l are integers, and n_{eff} is an effective refractive index that characterizes the waveguided modes sustained in the photoresist thin film. The crossing points between the R-W anomaly of the square lattice and the solution of equations relative to TE and TM modes (see details in Supporting Information, Figure S7, Supporting Information) allow us to identify the wavelength where the coupling

should occur (Figure 2A). In our case, the coupling is produced in a spectral region where TE and TM effective refractive index is very close to the substrate refractive index n_s , and the hybrid waveguided TM and TE modes were found at $\lambda = 604$ nm and $\lambda = 605.5$ nm, respectively.

Figure 2B shows the comparison between the simulated 0th-order transmission spectra of the cluster array in the presence and absence of a 250 nm thick layer of SU8. Since the system is not index-matched (i.e., the superstrate is air in both cases), the transmittance spectrum of the cluster array on glass (without a photoresist layer) does not show any appreciable diffractive or SLR mode.^[61] On the contrary, the cluster array simulated on top of the SU8 thin film shows a strong and sharp optical feature at 611 nm. The red shift compare to the positions predicted in Figure 2A is due to the localized plasmonic contribution of the cluster. Finally, we simulated the presence of RhB in the epoxy-resin matrix, which is clearly evidenced by the appearance of an intense minimum in the transmission spectrum at 567 nm (pink curve in Figure 2B). Moreover, the consequent slight increment of the optical losses of the system translates in a slightly broader and red-shifted SLR. Overall, these observations emphasize how the presence of narrow optical modes in the absence of a homogenous dielectric environment suggests the formation of hybrid waveguided-SLR modes, in contrast to pure SLR modes (Figure S11E, Supporting Information).^[62] The nature of the generated hybrid modes was characterized further by simulating the electric-field distribution maps at the associated wavelengths (Figure S6, Supporting Information).

Morphological and optical characterization of the prepared substrates is summarized in Figure 3. High magnification SEM analysis of the resulting silver plasmonic cluster arrays self-

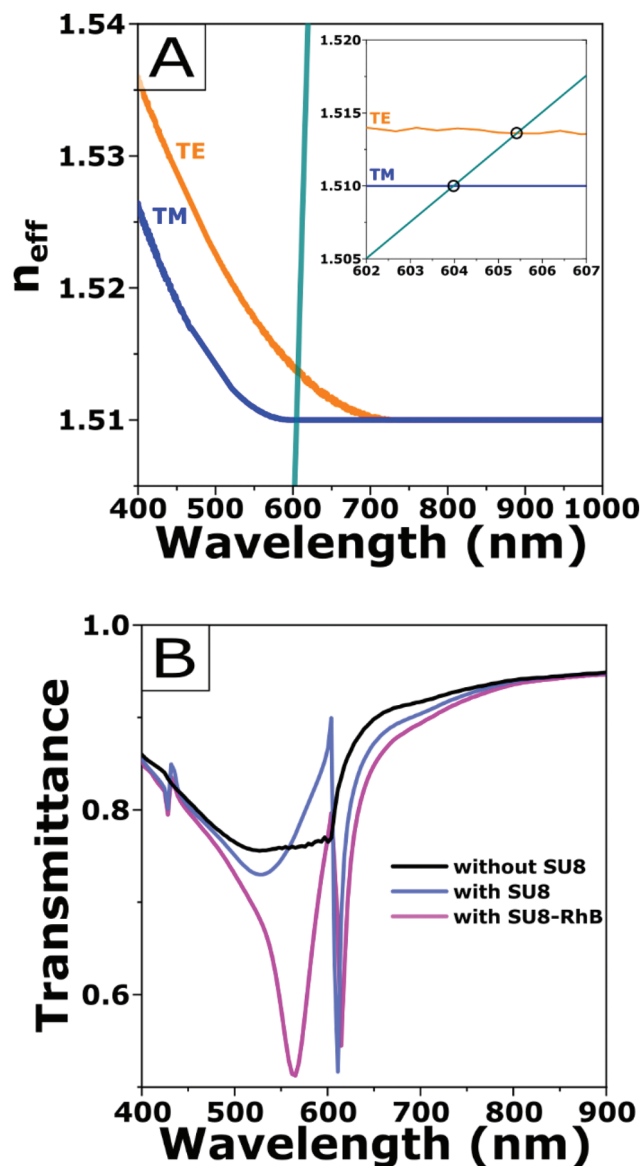


Figure 2. A) The graph displays the variation of the simulated TE and TM mode effective refractive index (n_{eff}) as a function of the wavelength (respectively the orange and the blue traces), and the spectral position of the first diffraction order of the R-W anomaly (cyan trace) for the case of a lattice period $\Lambda = 400$ nm. Inset: Zoom of the spectral region of interest. The crossing points between these modes (black circles at 604 and 605.5 nm) corresponds to the position where the coupling between the diffraction and the waveguide mode is expected, without considering the plasmonic contribution. B) Simulated transmission spectra showing the effect of the SU8 layer, with and without the dye, on the appearance of a narrow SLR signal. The electric-field distribution of the two hybrid modes can be found in Figure S6 (Supporting Information).

assembled onto RhB-SU8 layers with Λ of 400, 500, and 600 nm reveals that the clusters are composed of 1–5 layers of AgNPs Figure 3A–C. This variability in the number of layers is expected due to unavoidable concentration gradients during solvent evaporation. However, the resulting effect on the collective optical response of the arrays is expected to be minor, with the localized

plasmon band associated with the AgNP cluster remaining blue-shifted compared to the 0th diffraction (Figure S5A, Supporting Information). As can be seen in Figure 3G, different plasmonic arrays fabricated with increasing Λ from 400 to 500 and 600 nm show SLRs at 627, 752, and 909 nm, respectively, while the presence of RhB within the SU8 layer is evidenced by the transmission dip at 565 nm, corresponding to the absorption band of the dye. Overall, the combination of the high uniformity of the prepared plasmonic substrates and the presence of the thin SU8 layer translates into narrow SLRs,^[7] with the $\Lambda = 600$ nm sample reaching a remarkable Q -factor of 85. Importantly, the absence of any annealing or index matching step demonstrates the potential offered by colloidal plasmonic-based metasurfaces in creating new opportunities for the post-assembly modification of the optical cavity (e.g., dynamic interactions, ligand exchanges, and colloidal overgrowth steps).

To demonstrate the dispersive nature of the reported SLRs, transmission measurements were performed with varying incidence angles from 0° to 35° (angle resolution of 1°, Figure 3D–F) using an automated custom-built optical setup (Figure S3, Supporting Information). This characterization enables the direct observation of the various diffractive orders as they interact with the illumination angle-invariant plasmonic band associated with the AgNP clusters.^[57] Given the small refractive index mismatch between the SU8 ($n_1 = 1.6$) and the underlying glass coverslip ($n_2 = 1.52$) the hybrid waveguided-SLR modes are spectrally close, and due to the low coherence of our light source, they could not be distinguished in our transmittance measurements. As a consequence, the spectral positions of the hybrid modes can still be approximated by one of the R-W anomalies, which can be predicted from simple Bragg conditions, using an effective refractive index that takes into account the presence of both glass and SU8. For a square lattice array, this leads to:

$$1 - \left[\left(\frac{m\lambda_{RW}}{n_{eff}\Lambda} - \frac{n_{air}}{n_{eff}} \sin \theta_{inc} \cos \varphi_{inc} \right)^2 + \left(\frac{l\lambda_{RW}}{n_{eff}\Lambda} - \frac{n_{air}}{n_{eff}} \sin \theta_{inc} \sin \varphi_{inc} \right)^2 \right] = 0 \quad (1)$$

where Λ is the lattice period, n_{eff} is the effective refractive index, θ is the illumination angle with respect to the normal direction, φ is the azimuthal angle, and m and l are integers indicating the diffraction orders. The output light (0th transmission) by the designed photonic grating is subjected to Snell's law. The excellent agreement between the measured and predicted behavior of the SLRs shown in Figure 3D–F confirms the low optical losses within our systems.^[63] For all the lattice parameters, the SLRs associated with the first diffraction order present two degenerate lateral branches corresponding to the (1,0) order, red shifting for higher illumination angles, and the (-1,0) order, which instead blue shifts. The contour plots also highlight the presence of other degenerate branches at higher frequencies, corresponding to higher-order diffraction lines. The observation of these higher diffraction orders is yet another confirmation of the large-scale uniformity of the assembled arrays.

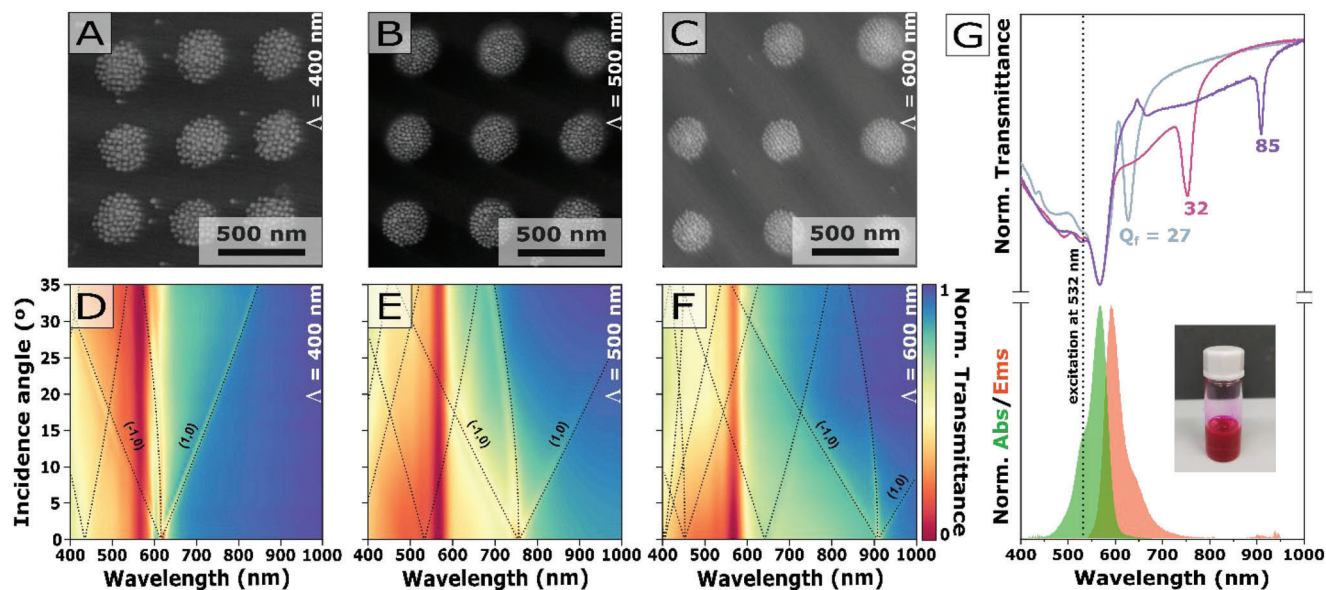


Figure 3. Characterization of the silver plasmonic arrays. A–F) Scanning electron microscopy measurements (A–C) and contour plots of the transmittance spectra of silver nanoparticle arrays as a function of the illumination angle (D–F), displayed as incident angle versus wavelength to facilitate comparison with panel G, with $\Lambda = 400$ (A,D), 500 (B,E), and 600 nm (C,F). The transmission spectra composing the contour plots were not normalized one by one, but simply scaled to the same value range to facilitate comparison between the three lattice parameters. The black dashed lines represent the predicted Rayleigh-Wood anomalies using equation (1). G) Normalized transmittance spectra at normal incidence (top) of the three lattice parameters (400 (light blue), 500 (pink), and 600 (purple) nm), and their comparison with the absorption (green) and emission (red) profiles of Rhodamine B (bottom) in SU8 (vial pictured in the inset).

2.3. Simulation of the Expected Emission Characteristics

The generation of stable lasing emission relies on both the absorption and emission characteristics of the system. On one side, it is important that the pumping frequency is absorbed effectively by the gain medium, which motivates the choice of RhB, a high-quantum yield dye.^[64] On the other hand, the process requires the existence of a radiative cavity mode overlapping with the gain medium emission bell, providing the optical feedback needed to achieve population inversion.^[65,66] The expected emission response of the system was simulated as shown in **Figure 4A**, considering a glass substrate ($n_{\text{glass}} = 1.51$), a layer of 250 nm of SU8 ($n_{\text{SU8}} = 1.6$), and a cluster of 25 nm NPs (\varnothing of 230 nm) individually covered with a 1 nm shell ($n_{\text{shell}} = 1.45$) to account for the PEG ligand shell of the colloids. The RhB was considered only as an absorber, and the complex refractive index was parametrized to fit with the experimental absorption measurement.

Using $\Lambda = 400$ nm as a model system, the lasing process was simulated using finite-difference time-domain (FDTD, Lumerical by Ansys) method, solving Maxwell's equations on a mesh grid with a semi-classical approach based on a four-level two electrons gain medium system (see Supporting Information, Figure S8–9).^[67,68] The system needs less than 10 ps from the initial excitation time to reach the steady state, where the populations of N_1 and N_2 remain constant. After 5 ps, the system reaches population inversion between the excited and the ground state, leading to the emergence of a lasing peak centered at 610 nm (retrieved by Fourier transforming into time-domain the filtered monitor signal placed in the gain media), which is spectrally overlapping with the simulated hybrid waveguided-SLRs (Figure 4B).

In order to visualize all the available photonic and plasmonic modes within the first Brillouin zone, we simulated a band diagram for each of the three lattice parameters used in this study, taking into consideration an SU8 layer of 250 nm, and the presence of RhB. (Figure 4C). The diffractive features, corresponding to both TE and TM polarizations, appear highlighted in blue over the other sources of optical losses (light-yellow background), including the absorption by RhB and the AgNPs. Of the identified modes, only the ones lying outside of the line of light (represented by the grey shadowed area in Figure 4C),^[13] can couple to the far field and are not confined to the plane of the array. The crossing points between these modes identify the ideal conditions for optical loss compensation, and consequently the promotion of lasing emission. Note that the angular displacements of the lattice resonances in terms of illumination angle versus wavelength (Figure 3D–F) agree with what was simulated as energy versus in-plane wavevector k_{\parallel} in the band dispersion diagram, based on the relations $E = h \cdot c / \lambda$ and $k_{\parallel} = (2\pi / \lambda) \cdot \sin \theta$.

For $\Lambda = 400$ nm, the crossing point of the 1st order R–W anomalies with four-fold degeneracy can be distinguished at $k_{\parallel} = 0$, at the high symmetry point Γ of the first Brillouin zone (pink arrow in Figure 4C-i). The presence of these resonant modes around 600 nm helps the out-coupling of the light to the far field, ultimately lowering the lasing emission threshold normal to the plane of the lattice. In the $\Lambda = 500$ nm case, two crossing points in the band diagram can be identified as off-normal to the plane of the lattice (pink arrows in Figure 4C-ii), respectively along the Γ -X direction, and the M- Γ direction. Finally, for $\Lambda = 600$ nm the crossing point is located once again off-normal at the Γ -X direction (Figure 4C-iii).

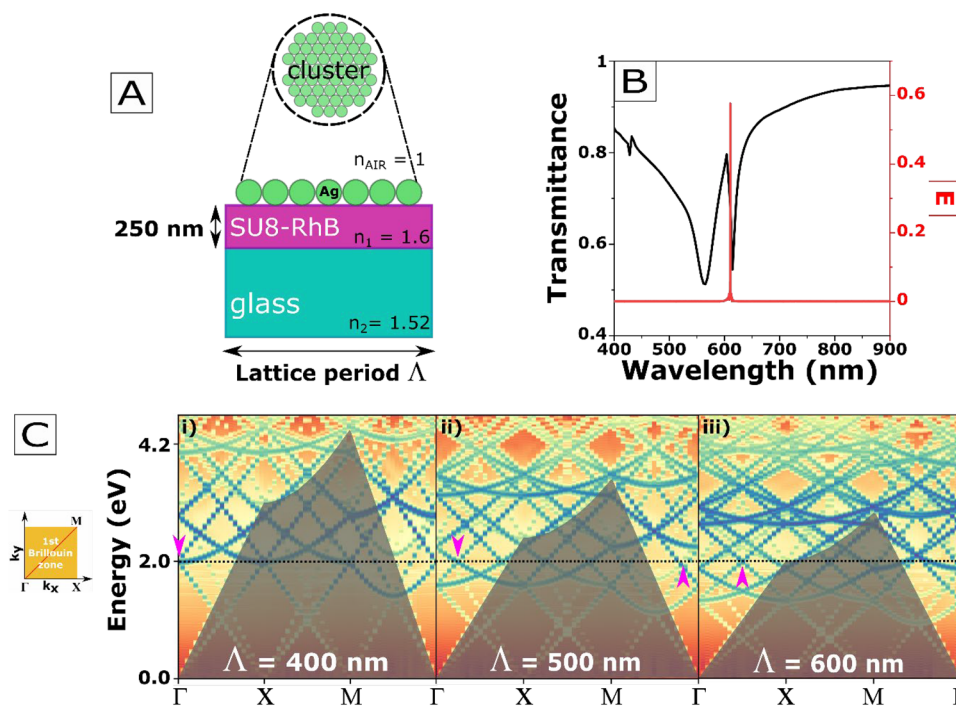


Figure 4. Theoretical modeling of the system. A) Schematic of the simulated system unitary cell, composed by a cluster made of a single layer of AgNPs. B) Spectral overlap between simulated transmittance spectrum and lasing emission (610 nm) of a $\Lambda = 400$ nm sample, obtained as the inverse Fourier transform of the frequency-filtered signals (E), see Supporting Information. C) Band diagrams of the three lattice parameters Λ , showing all possible modes as function of frequency and in-plane wavevector k_{\parallel} of incident light; the borders of the grey shadowed areas delimitate the light cones ($\omega = c \cdot |k_{\parallel}|$); the horizontal dotted lines represent the maximum of the dye emission bell, and the pink arrows indicate some crossing-points representing the frequency at which lasing is observed for the three lattice periods.

2.4. Characterization of the Emission Behavior of $\Lambda = 400$ nm

Experimentally, the lasing capability of our samples was characterized using a customized optical setup. Briefly, a pump laser (532 nm, pulse width 1.5 ns) was controlled through a customized software, allowing the selection of the number of pulses and repetition rate by triggering the laser externally. We selected a low repetition rate (100 Hz), to avoid accumulation in the triplet states of the dye molecules,^[15] and two excitation pulses per measurement. These conditions also allow us to limit photobleaching effects, and to perform a complete set of measurements in the same spot on the sample. The pump's average power was recorded before each measurement using a power meter. When a Λ of 400 nm was used, the appearance of a narrow emission line (FWHM ≈ 5 nm, close to the spectrometer resolution) was confirmed normal to the surface at 610 nm in transversal electromagnetic (TEM) configuration (Figure 5A).

The pump power density (mJ mm^{-2}) was recorded in the same position on the sample, showing the anticipated threshold behavior characteristic of lasing emission with a clear change in slope at 0.3 mJ/mm^2 (Figure 5B-C). The collected data are in excellent agreement with the predictions of both the FDTD simulations and the band diagram (Figure 4B,C, respectively). Superimposing the lasing emission with the transmittance spectra, a slight blue shift (< 10 nm) can be observed when compared to the SLR position (Figure 5A). This discrepancy can be justified considering small variations in the SU8 layer thickness and the lattice parameter, as well as the incoherency of the used

white light source. To confirm the stimulated emission behavior, both divergence and polarization were measured. As expected, the recorded lasing emission is highly directional (divergence angle $< 1.5^\circ$, Figure 5D), and presents clear polarization behavior that fits well with a sine squared function, as predicted by Malus' law (Figure 5E).^[7,69] Overall, the formation of a narrow emission profile characterized by a clear threshold behavior, linear polarization dependence, small divergence, and high intensity (factor 10^4 above PL intensity, Figure S4, Supporting Information) clearly suggests the emergence of a stimulated emission, in accordance with the most recent indication by the community.^[70] The prepared devices maintained performance over the course of one month before starting to slowly degrade, probably due to the oxidation of the silver clusters, reducing the efficiency of the optical cavity.

The absence of lasing activity outside of the patterned area and in the presence of randomly distributed AgNPs confirms the central role played by the plasmonic array (Figure S12, Supporting Information). The mechanism underlying the enhanced stimulated emission could involve the combination of plasmonic and photonic effects due to the hybrid nature of SLRs.^[71] Specifically, the presence of plasmonic surfaces can decrease the lasing thresholds by strong electromagnetic confinement and provide enhancement of the optical emission due to changes in the local density of states.^[72] On the other hand, the optical feedback provided by the photonic grating could be further enhanced by the high scattering cross-section of the metallic cluster of NPs.^[15] Moreover, the thin SU8 layer and the supported hybrid

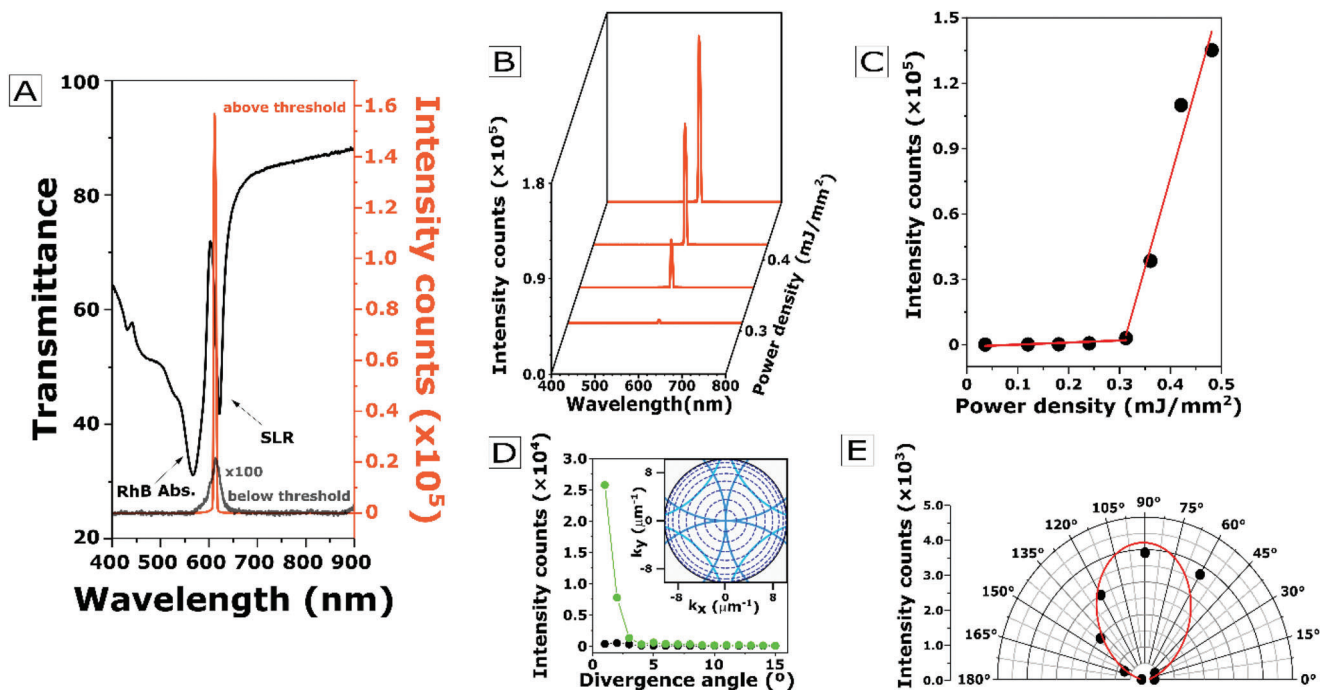


Figure 5. Lasing characterization of the $\Lambda = 400$ nm sample. A) Spectral overlap between the experimental lasing emission above (orange) and below (grey) threshold, and transmittance of the plasmonic array. B) Waterfall graph of the lasing emission as a function of pump power density. C) Peak emission intensity versus pump power density. D) Emission divergence study, confirming normal emission and high directionality of the lasing emission (green trace) in comparison to normal fluorescence (black trace). Inset: k-space plot of the Rayleigh-Wood anomalies (solid blue lines) distributed in all angular directions, where the dotted circles represent the illumination angles intervals (from 10° to 80°) for azimuthal angles in the full 2π range. E) Peak intensity of the measured laser emission as a function of the angle α between the plane of the polarizer and the incident plane arising from the sample. The red line shows a $\sin^2(\alpha)$ fit of the data points.

waveguided-SLR modes can operate synergistically with these photonic effects adding new degrees to tune the optical properties of the system.

2.5. Off-Normal Emission: $\Lambda = 500$ and 600 nm

The generation of lasing activity using waveguided-SLRs offers the opportunity to exploit their angular dispersion to access off-normal lasing emission by modifying the geometry of the photonic structure.^[23,60] Here, we tested the emission performance as a function of Λ , taking advantage of template-assisted self-assembly versatility. In the case of $\Lambda = 500$ nm (see **Figure 6**), the band diagram (Figure 4C) predicts that the $(\mp 1,0)$ diffraction modes of the square array would cross the emission maximum of the gain media (≈ 600 nm) around 17° , yielding a stimulated emission at an off-normal direction, as can also be observed in the k-space plot (Figure 6D). The intensity difference between the two lasing conditions ($+17^\circ$ and -15°) is likely due to photobleaching effects on the dye molecules due to the higher intensity pumping imposed by the higher threshold compared to the case of normal emission. Our experimental results are in excellent agreement with the theoretical predictions. Lasing emission was recorded at 602 nm with an FWHM of 10 nm, at both off-normal directions of 17° and -15° (Figure 6A), with a small angular divergence ($<1.5^\circ$, Figure 6C). The spectral overlapping of the lasing emission with the transmittance spectra recorded at

17° (Figure 6A) confirmed a similar correlation with the hybrid waveguided-SLR as the one shown in Figure 5A. Compared to the $\Lambda = 400$ nm, we found a 4 times higher threshold (1.2 mJ/mm², Figure 6B), which can be attributed to the variation of $k_{||}$ from 0 to higher values, increasing both the scattering cross-section and the radiative losses of the optical modes of the plasmonic arrays.^[15]

For $\Lambda = 600$ nm, both the transmittance spectrum (Figure 3G) and divergence contour plot (Figure 3F) show the presence of two diffracted orders, with one dip at 667 nm and one at 910 nm. According to the band diagram reported in Figure 4C, this leads to two different conditions under which lasing can be achieved. On one hand, the lattice resonance at 910 nm couples with the first order of diffraction at an angle of $\sim 40^\circ$, resulting in a predicted off-normal emission. Alternatively, a stimulated emission at smaller off-normal angles ($\sim 8^\circ$) could be generated by exploiting the second order diffraction modes at 667 nm.

Experimental constraints prevent us from collecting emission signals at angles $> 35^\circ$, and we were unable to detect any lasing activity around 8° . We hypothesize that higher-quality plasmonic arrays are required for the emergence of second order diffraction modes efficient enough in order to promote stimulated emission. Interestingly, at normal incidence, we observed a threshold behavior (Figure 7B) and the appearance of a sharp peak at 605 nm with an FWHM of 8 nm (Figure 7A). However, the lack of polarization dependency of the emission (Figure 7C), and a much lower intensity compared to the cases of $\Lambda = 400$ and

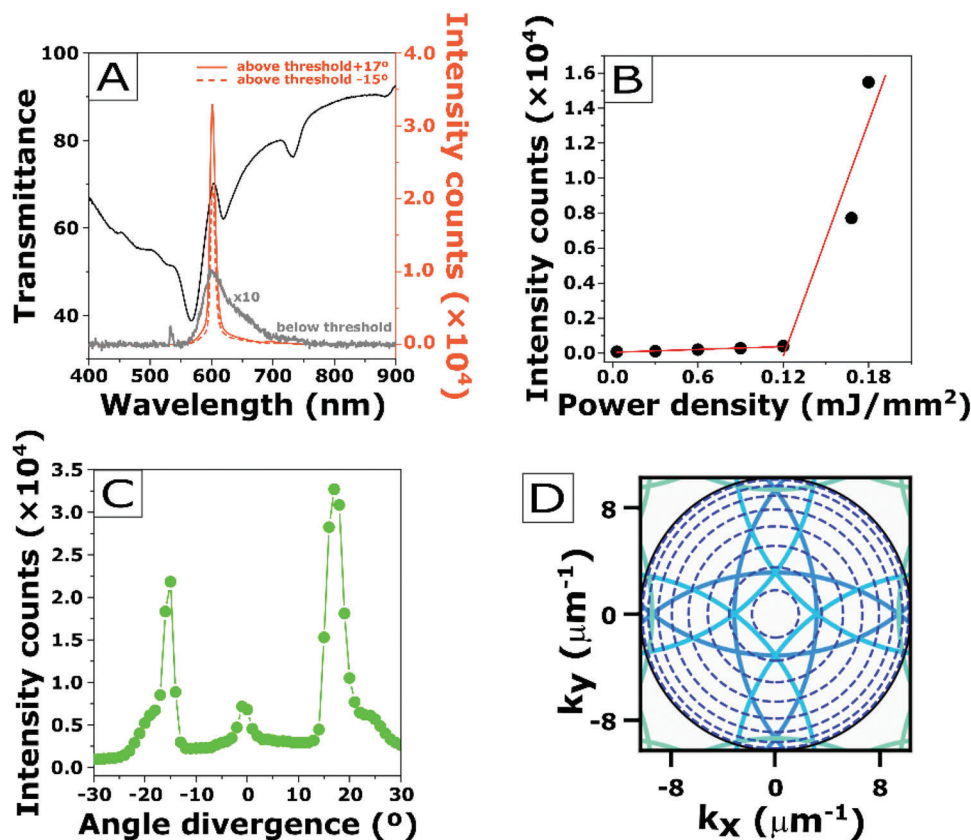


Figure 6. Lasing characterization of samples with $\Lambda = 500$ nm. A) Spectral overlap between the transmittance of the plasmonic array measured at 17° (black line), and the emission below (light grey line) and above (orange lines) threshold for both 17° and -15° (solid and dotted lines, respectively). B) Peak emission intensity versus pump power density to show the threshold behavior of the stimulated emission. C) Angle divergence characterization of the lasing emission (from -30° to $+30^\circ$). Two clear emission peaks emerge at 17° and -15° . D) k-space plot of the Rayleigh-Wood anomalies (solid blue lines) distributed in all angular directions, where the dotted circles represent the illumination angles intervals (from 10° to 80°) for azimuthal angles in the full 2π range.

500 nm, suggest that this observation should be interpreted as amplified spontaneous emission (ASE) originated from exciton re-absorption by the dye molecules. Alternatively, we attempted to collect the signal using a 100 \times objective. This enables the identification of a lasing emission, but at the same time makes it impossible to univocally identify the mode responsible for the stimulated emission (Figure S13, Supporting Information) due to the high numerical aperture of the objective ($NA = 0.8$).

3. Conclusions

In conclusion, this work demonstrates the use of a low-cost, versatile, and highly scalable technique such as template-assisted self-assembly for the preparation of high-quality plasmonic-based metasurfaces to promote nonlinear optical emission phenomena. In the proposed lasing architectures, the gain medium layer serves as the substrate for the construction of the optical cavity, exploiting the hydrophobicity of the photoresist to improve the quality of the assembled plasmonic arrays and take advantage of generating hybrid waveguided-SLR modes. A threshold of 0.3 mJ mm^{-2} was achieved using a Λ of 400 nm, and we expect that further improvements in the optical cavity and the implementation of a more efficient and photostable gain media could

potentially lead to lower thresholds and improved performance in the future. Nonetheless, the easy fabrication process (avoiding metal evaporation, annealing treatment, or index matching overlayer) and the versatility offered by template-assisted self-assembly are important steps forward in the context of non-linear optics. These advantages were demonstrated by tuning the lasing emission angle with the simple modification of the lattice parameter of the array, taking advantage of the delocalized nature of the hybrid modes. The recorded results are supported by numerical simulations and theoretical models, confirming that lasing was indeed achieved in the different conditions explored. Our fabrication methodology does not require the support of clean room facilities. Moreover, the presence of an exposed optical cavity opens the door to effective and straightforward chemical modification of the plasmonic metasurface. This aspect represents an interesting novelty compared to high-performance architectures fabricated via standard lithographic approaches, making these types of architectures more flexible for applications in different fields, such as photocatalysis,^[74,75] biosensing,^[76,77] energy conversion,^[78] and structural color display devices.^[79] Finally, the implementation of the proposed lasing scheme with more efficient emitter (e.g., quantum dots or fluorescent polymers) and more complex photonic structures can potentially

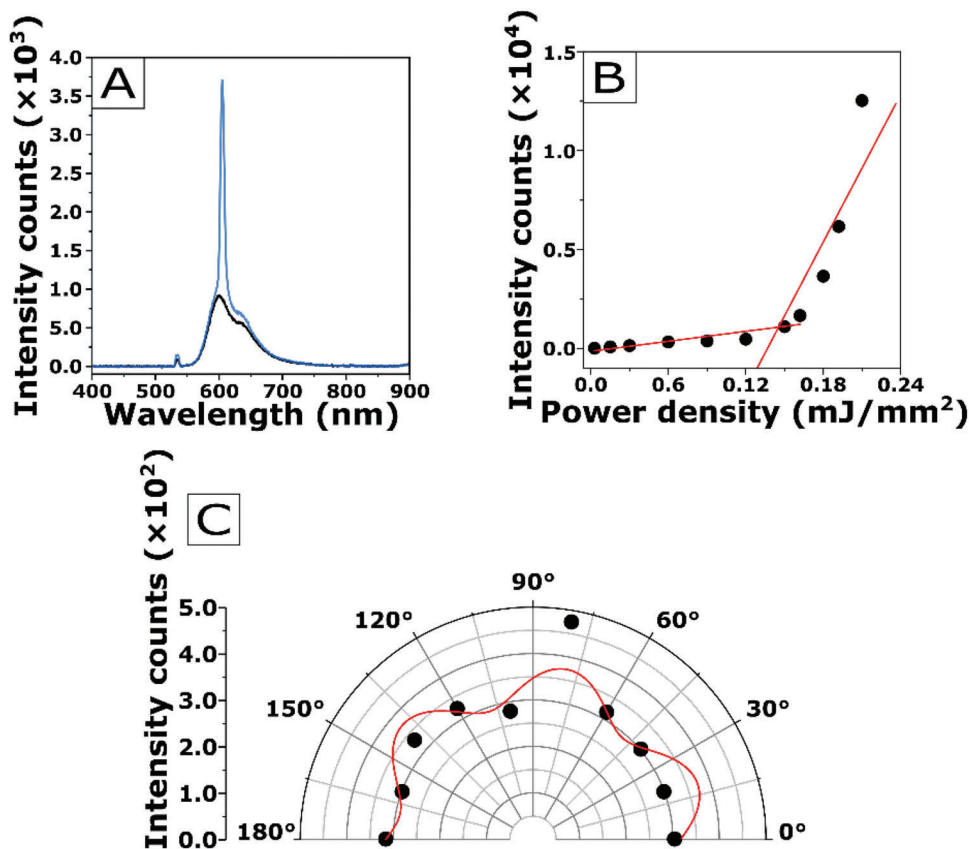


Figure 7. Lasing characterization of samples with $\Lambda = 600$ nm. A) Emission of the sample with lattice period of 600 nm at normal incidence. Above threshold (light blue line) the emerged peak can be interpreted as amplified spontaneous emission (ASE). B) Peak emission intensity versus pump power density to show the threshold behavior, which is expected in the case of ASE. C) Peak intensity of the measured emission as a function of the polarizer angle (from 0° to 180°). The absence of a clear polarization is a strong indicator of ASE instead of lasing emission.

lead to an improvement in the device performance, closing the gap with more established but less versatile architectures.

4. Experimental Section

Materials: For the synthesis of silver nanoparticles, the used reagents are: silver nitrate (AgNO_3 ; 99%, CAS: 7761-88-8), sodium citrate tribasic dihydrated (SC, $\geq 99.0\%$, CAS: 6132-04-3); tannic acid (TA, CAS: 1401-55-4); poly(ethylene glycol) methyl ether thiol (PEG, MW 2000 g mol^{-1}); hexadecyltrimethylammonium chloride (CTAC, 25 wt.% in water, CAS: 112-02-7), were purchased from Sigma Aldrich. For the silanization of the masters trichloro (1H,1H,2H,2H-perfluorooctyl) silane (97%, CAS: 78560-45-9) was purchased from Sigma Aldrich. Polydimethylsiloxane (PDMS, Sylgard 184) used for the stamps was purchased from Dow Corning (Michigan, USA). The hard PDMS (h-PDMS) was prepared by components purchased from Gelest (CymitQuimica, Spain): (7.0–8.0% vinylmethylsiloxane)-dimethylsiloxane copolymer, trimethylsiloxy terminated (CAS: 67762-94-1), 1,3,5,7-tetramethylcyclotetrasiloxane (95%, CAS: 2370-88-9), platinum-divinyltetramethyldisiloxane complex (2% in Pt in xylene, CAS: 68478-92-2), and (25–35% methylhydrosiloxane)-dimethylsiloxane copolymer, trimethylsiloxane terminated (CAS: 68037-59-2). The glass substrates were cleaned using a piranha solution prepared by mixing 95–98% w/w sulfuric acid (CAS: 7664-93-9), and 30% w/w hydrogen peroxide (CAS: 7722-84-1) in a 3:1 ratio, purchased from Fisher Scientific. Rhodamine B dye powder was purchased from Sigma Aldrich (RhB, CAS 81-89-9; MW 479.01 g mol^{-1}). The negative photoresist SU8-2000.5 (14% in thinner) is

purchased from KAYAKU Advanced Materials (Westborough, MA 01581). The SU8-2000 thinner was purchased from MicroCHEM (Westborough, MA 01581).

Synthesis of Silver Nanoparticles: Silver spherical nanoparticles (Ag-NPs) with an average diameter of 23 ± 3 nm were synthesized using a method previously reported by Bastus et al.,^[80] with slight modifications. First, the stock solutions of silver nitrate (AgNO_3) 25 mM, sodium citrate (SC) 25 mM, and tannic acid (TA) 2.5 mM were prepared. Afterward, 200 mL of an aqueous solution of SC (5 mM) and 2 mL of TA stock solution (2.5 mM) were mixed under vigorous stirring in a three-neck round-bottomed flask, immersed in a silicon oil bath. The evaporation of the solvent was prevented using a condenser, and the temperature of the system was monitored and controlled with a digital thermometer placed in the oil bath. The temperature was increased until vigorous boiling, then 2 mL of the AgNO_3 stock solution (25 mM) was added to the solution. The color of the growth mixture changed rapidly from yellow, due to the presence of TA, to dark brown due to the formation of Ag seeds close to 10 nm in diameter (LSPR maximum at 402 nm). The size of the seeds could be controlled by adjusting the concentration of the TA. After the formation of the Ag seeds was completed (5 min), the reaction was cooled to 90 °C to begin the nanoparticle growth. Once the mixture reached the desired temperature, 200 μL of SC (25 mM), 500 μL of TA (2.5 mM), and 500 μL of AgNO_3 were injected into the growth mixture, with a delay time of ≈ 1 min from each other. After 15 min, an aliquot of 1 mL was extracted for UV–vis characterizations. The position of the absorbance spectrum peak was taken by using a UV–vis spectrophotometer (HITACHI U-3010), to estimate the average AgNP diameter. In a typical example reported in Figure

S1C (Supporting Information), the plasmon band presents a maximum at 406 nm, indicating that AgNPs have reached the desired dimension with a single growth step (≈ 25 nm). If this were not the case, more growth steps can be repeated until the desired dimension is achieved, adding 200 μL of SC (25 mM), 500 μL of TA (2.5 mM), and 500 μL of AgNO_3 each time. Once the growth is complete, the colloidal suspension was centrifuged three times (15000 rpm for 30 min) to eliminate the reagent leftovers and to concentrate the particles from 200 mL to less than 2 mL. Once concentrated, AgNPs were functionalized with poly (ethylene glycol) methyl ether thiol (PEG) with a molecular weight $\text{MW} = 2000 \text{ g mol}^{-1}$. The PEG is first weighted to reach a final concentration of 1 mg mL^{-1} in the colloidal suspension, then dissolved in a small volume of Milli-Q water (typically $< 200 \mu\text{L}$), and finally added drop-by-drop under vigorous stirring to the concentrated AgNPs colloid. The mixture was left stirring overnight at room temperature to ensure complete functionalization of the surface by the thiolated polymer. The following day, the excess of PEG was removed with two centrifugation steps (15000 rpm for 30 min), and the colloid was finally suspended in a mixture of Milli-Q water and ethanol in a 6:4 ratio containing hexadecyltrimethylammonium chloride (final [CTAC] = $50 \mu\text{M}$).^[9] The dimension of the nanoparticles was confirmed by transmission electron microscopy analysis (Figure S1A, Supporting Information) using a JEOL 1210 (Tokyo, Japan) operating at 120 kV using carbon-coated 400 square mesh copper grids. The concentration of the AgNPs was characterized by their extinction spectra, and for all the preparation used in this manuscript, the extinction maxima at 406 nm were set at 0.5, with a dilution factor of 1000 (i.e., real extinction value would be 500).

Nanoimprinting: Preparation of the Original Master Replicas with Ormostamp: First, Ormostamp replicas were obtained from the original silicon masters purchased from EULITHA (Switzerland). In the context of this work, the used masters were arrays of cylindrical holes prepared on silicon substrates with lattice periods of 400, 500, and 600 nm over 49 mm^2 areas (Table S1, Supporting Information). The silicon masters were treated by silanization via chemical vapor deposition of perfluorooctyl-trichlorosilane, under a vacuum in a desiccator for 30 min. This treatment protects the masters and avoid the Ormostamp to stick permanently to the silicon surface. Once the deposition was completed, the masters were rinsed with acetone and heated at 120°C for 20 min to remove all the silane leftovers. Then, a drop of Ormostamp photoresist was placed directly on top of the silanized silicon master. A cleaned glass slide, pre-treated with UV-O_3 for 20 min, was gently superimposed on the master, making sure that no bubbles remain trapped between the glass and the Ormostamp layer. The photoresist was then activated by exposure to direct UV-light for 10 min. Finally, cross-linking was favored by placing the substrates on a hot plate and applying a temperature ramp from 60 to 150°C (6°C min^{-1}) for 30 min. Apart from the curing of the photoresist, the difference of thermal expansion coefficient between the photoresist and silicon induces the Ormostamp to easily detach from the silicon master. At the end of this process, Ormostamp patterned as pillar arrays (negative master) can be used to prepare replicas of the original masters by nanoimprint lithography (operative masters, see below).

Nanoimprinting: Preparation of the h-PDMS Molds: The Ormostamps master was replicated using hard (h-)PDMS, in order to prevent the collapse of the structure during the demolding procedure. The h-PDMS composite was used in a thickness of a few microns deposited via drop casting, while the backbone of the replica was composed of a soft (s-)PDMS to ensure enough flexibility. Specifically, the h-PDMS mixture was prepared by adding under vigorous stirring: 1.7 g vinylmethylsiloxane, 50 μL of 1,3,5,7-tetracyclotrisiloxane, 4 μL of Pt catalyst, 550 μL of hydroxyl siloxane, and 2 mL of toluene. The sequence of addition should be performed as fast as possible since the h-PDMS mixture will immediately start to cure; due to toluene quick evaporation rate the obtained mixture can be used for approximately 15 min, after which the mixture begins to solidify. The mixture was drop cast on top of the patterned area and spread over the entire surface by using a compressed air gun, ensuring to not leave air microbubbles trapped in the layer. This process is repeated 3 times for each sample. The substrates were left for 30 min at room temperature and then on a hot plate at 60°C for 1 h to evaporate all the toluene. Afterward, s-PDMS was prepared and poured on the masters as described below and left overnight

to cure using a temperature ramp of 60, 80, and 120°C . This process can be repeated several times, meaning that from a single silicon master is possible to obtain a virtually unlimited number of PDMS templates.

Nanoimprinting: Preparation of Operative Masters with SU8 2000.5: The h-PDMS stamps were used to replicate the original silicon masters on a thin SU8 layer via nanoimprint lithography. The epoxy based negative photoresist was spin coated (2000 rpm, 1000 rpm/s, 30 s) on cleaned glass or silica wafer and then placed on a hot plate. The temperature was increased to 120°C and the h-PDMS mold was superimposed and gently pressed into the SU8 layer: rapidly, the mold deforms the epoxy layer. The substrates were left to cool down at room temperature. Afterward, it was possible to proceed with the demolding, leaving a nanopatterned area of pillars. Finally, the obtained patterned SU8 layers were exposed for 10 min to direct UV-light, and post-baked for 30 min on a hot plate at 150°C .

Template-Assisted Self-Assembly of Silver Colloids: Preparation of s-PDMS Molds: s-PDMS templates were used for the AgNPs self-assembly, resulting in much more flexible and durable molds, even after several uses (typically 10–15 preparations). The polymer mixture is prepared by combining a 10:1 ratio of monomer and curing agent in falcon tubes of 50 mL. The two components were mixed very vigorously for several minutes, to ensure their homogeneous distribution. To remove the air bubbles, the tubes were centrifuged at 3200 rpm for 5 min. Alternatively, it was possible to remove the air bubbles leaving the s-PDMS mixture to degas inside a desiccator for approximately 1 h. Finally, the mixture was poured onto the silanized operative masters (pillars). After curing overnight in the oven at 60°C or on a hot plate with a temperature ramp of 60, 80, and 120°C for 1 h, it was possible to proceed with demolding, resulting in cylindrical nano-holes patterned s-PDMS.

Template-Assisted Self-Assembly of Silver Colloids: Sample Preparation: A drop of AgNPs (1 μL) was placed on the center of the substrate (Figure S2, Supporting Information). The concentration of the NPs was chosen by UV-vis measures, in order to use for all samples the same amount of volume was dropped on the substrate, ensuring the reproducibility of arrays quality (defect-less structures and no particles outside the cluster area, Figure S10, Supporting Information). Immediately, a PDMS mold patterned as cylindrical hole square arrays with the selected lattice parameter was superimposed on the dispersed nanoparticles. The solvent evaporation promotes the self-assembly of the AgNPs into a plasmonic nanocluster array. The close packing of the particles within each cluster is guided by the shape and size of the cylindrical holes by the nanoparticle concentration, the solvent composition, and the CTAC concentration. After drying overnight, the sample was ready for the demolding step. The final appearance of the sample is the one shown in Figure 1B in the main text. Every sample was analyzed by scanning electron microscopy, using a FEI QUANTA 200 Electrons Field Emission Gun, operating between 5 and 15 kV in a low vacuum underwater atmosphere (60 Pa).

Template-Assisted Self-Assembly: Preparation of the Lasing Substrates: Rhodamine B (5.25 mg) was dissolved in 1 mL of SU8-2000 thinner, and mixed in a 1:1 ratio with SU8 2000.5 epoxy-based negative photoresist (final concentration of 2.8% w/w assuming complete evaporation of the thinner at the end of the preparation).^[51] An ultrasonic bath (Branson 2800, for 15 min) was used to facilitate the dissolution of RhB. The mixture was then spin coated (two steps receipt: 500 rpm, 100 rpm/s, 10 s and 2000 rpm, 300 rpm/s, 30 s) on a 20×20 mm cleaned glass coverslip. Samples were pre-baked at 60°C for 2 min and 95°C for 5 min to eliminate solvent residues. The sample was then exposed for 25 min under UV light and then hard-baked with a temperature ramp: 95°C for 5 min, 150°C for 10 min, and 180°C for 10 min.^[81] The final thickness reached for the SU8 layer is $t = 250$ nm, confirmed by interferometry measurements (Figure S2, Supporting Information) taken with an FTIR spectrometer (Vertex 70, Bruker) connected to an optical microscope (Hyperion, Bruker).

Angular Displacement with Optical Measurements: The experimental optical setup was customized using LabVIEW licensed programs to automatize the measurements. The plasmonic patterned area was illuminated at normal incidence using white light, produced by a Tungsten Halogen Lamp (Ocean Optics, HL-2000-HP, Florida, USA) corrected by two filters (Edmund Optics, SCHOTT BG64, and Thorlabs, SRF11) to increase counts in the UV and NIR region. The light was focused on the sample

and collected using two achromatic doublet lenses ($f = 100.00$ mm and $f = 50.00$ mm). The detection system was mounted on a rotational optical breadboard (Thorlabs, RBB12A, New Jersey, USA), while the sample holder was anchored on a rotational stage ($\varnothing = 50$ mm) with resonant piezoelectric motors (Thorlabs, ELL18/M) equipped with an interface board controlled by software. The two-rotation system rotates concentrically to one another. This allowed the automatic rotation of the illumination angle θ (from 0° to 35°) of the sample, with a resolution of 0.1° . The sample was mounted vertically and oriented along the high symmetry direction of the clusters on a custom-made sample holder, which enables to control the azimuthal angle φ ($\pm 3^\circ$) alignment. The transmitted light was collected using a fiber-coupled spectrophotometer (Ocean Optics, QEPro-FL) with a range of detection 380–1200 nm. The described setup was used for all transmittance measurements of the manuscript.

Lasing Characterization: The 2D AgNPs cluster arrays assembled on a layer of gain media were optically pumped at normal incidence using a nanoseconds-pulsed green laser (CryLaS GmbH, Ostendstrasse 25, D-12459 Berlin, Germany), peaked at 532 nm, with a repetition rate of 100 Hz, and vertically polarized. By using an external trigger, the pump laser output was set at 2 pulses with a repetition rate of 100 Hz. To identify the lasing threshold, the laser power was increased from $4 \mu\text{W}$ up to $500 \mu\text{W}$, monitored by using a power meter console (Thorlabs PM100D) coupled to a standard photodiode power sensor (Thorlabs S121C). The experimental hardware is the same used for the angular characterization, except for a $10\times$ objective lens ($\text{NA} = 0.25$, $\text{WD} = 12.1$ mm) on the illumination path, to focalize the light in a small area on the pattern (diameter: $46.0 \pm 0.4 \mu\text{m}$, measured using a beam profiler BP209-VIS/M, Figure S3, Supporting Information). The produced photoluminescence was collected directly by a fiber coupled to a spectrophotometer (Ocean Optics, QEPro-FL) by using a reflective collimator (Thorlabs, RC08SMA-P01) as shown in Figure S3D, and a long pass edge filter with high transmission (Semrock Edge basic BLP01-532R-25) was used to block the pump laser-line. The entire hardware was connected to a workstation and a customized LabView program was used to manage the experiment.

Computational Methods: Simulations were performed using finite differences in the time domain (FDTD) implemented in the 3D Electromagnetic Simulator of Lumerical (FDTD solutions, Ansys). The calculations solve Maxwell's equations on a non-uniform mesh grid, with a minimum step size of 1 nm close to each NPs and diminishing the step up to 0.3 nm in the inter-particle hot spots regions. In addition, a conformational variant refinement was used considering the presence of the dielectric/metal interface. The fluorescence spectra were fitted using a model previously implemented by the authors.^[67]

Supporting Information

Supporting Information is available from the Wiley Online Library or from the author.

Acknowledgements

The authors would like to thank Dr. Martí Gibert Roca for his help in the realization of the optical setup and the dedicated software, as well as Dr. Sebastián Reparaz and Kai Xu for their assistance in the lifetime measurements. Y.C. acknowledges the auspices of the UAB material science doctoral program. This project received funding from the Spanish Ministerio de Ciencia e Innovación through grants, PDC2021-121475-I00/AEI/10.13039/501100011033 by the "European Union" NextGenerationEU/PRTR, PID2019-106860GB-I00/AEI/10.13039/501100011033 and FUNFUTURE (CEX2019-000917-S), in the framework of the Spanish Severo Ochoa Centre of Excellence program. L.S. and Y.C.'s research is supported by the 2020 Post-doctoral Junior Leader-Incoming Fellowship by "La Caixa" Foundation (ID 100010434, fellowship code LCF/BQ/PI20/11760028), and from a 2022 Leonardo Grant for Researchers and Cultural Creators, BBVA Foundation.

Conflict of Interest

The authors declare no conflict of interest.

Author Contributions

The experiments were designed by Y.C., J.M.C., L.S., and A.M.; Y.C. designed and optimized nanoparticle synthesis, self-assembly, and sample fabrication; N.P. designed and performed the simulations. Data were collected by Y.C. and J.M.C.; figures were prepared by Y.C.; and the manuscript was written by Y.C., with assistance from all other authors. All authors have given approval to the final version of the manuscript.

Data Availability Statement

The data that support the findings of this study are available from the corresponding author upon reasonable request.

Keywords

lasing, lattice plasmon resonance, plasmonic metasurfaces, silver nanoparticles, stimulated emission, template-assisted self-assembly

Received: May 2, 2023
Published online: June 30, 2023

- [1] L. Scarabelli, *Pure Appl. Chem.* **2018**, *90*, 1393.
- [2] K. L. Kelly, E. Coronado, L. L. Zhao, G. C. Schatz, *J. Phys. Chem. B* **2003**, *107*, 668.
- [3] U. Kreibig, M. Vollmer, In *Optical Properties of Metal Clusters*, Kreibig, U., Vollmer, M., Eds., Springer Series in Materials Science, Springer, Berlin, Heidelberg, **1995**, pp. 1–12, https://doi.org/10.1007/978-3-662-09109-8_1.
- [4] S. R. K. Rodriguez, M. C. Schaafsma, A. Berrier, J. G. Rivas, *Phys. B* **2012**, *407*, 4081.
- [5] A. A. Darweesh, S. J. Bauman, D. T. Debu, J. B. Herzog, *Nanomaterials* **2018**, *8*, 809.
- [6] V. G. Kravets, A. V. Kabashin, W. L. Barnes, A. N. Grigorenko, *Chem. Rev.* **2018**, *118*, 5912.
- [7] S. Zou, N. Janel, G. C. Schatz, *J. Chem. Phys.* **2004**, *120*, 10871.
- [8] M. Dridi, G. C. Schatz, *J. Opt. Soc. Am. B* **2015**, *32*, 818.
- [9] C. Matricardi, C. Hanske, J. L. Garcia-Pomar, J. Langer, A. Mihi, L. M. G. Liz-Marzán, *ACS Nano* **2018**, *12*, 8531.
- [10] J. Z. Zhang, C. Noguez, *Plasmonics* **2008**, *3*, 127.
- [11] M. Charconnet, C. Kuttner, J. Plou, J. L. Garcia-Pomar, A. Mihi, L. M. Liz-Marzán, A. Seifert, *Small Methods* **2021**, *5*, 2100453.
- [12] A. F. Koenderink, *ACS Nano* **2019**, *13*, 7377.
- [13] J. Guan, M. R. Bourgeois, R. Li, J. Hu, R. D. Schaller, G. C. Schatz, T. W. Odom, *ACS Nano* **2021**, *15*, 5567.
- [14] A. Yang, T. B. Hoang, M. Dridi, C. Deeb, M. H. Mikkelsen, G. C. Schatz, T. W. Odom, *Nat. Commun.* **2015**, *6*, 6939.
- [15] W. Zhou, M. Dridi, J. Y. Suh, C. H. Kim, D. T. Co, M. R. Wasielewski, G. C. Schatz, T. W. Odom, *Nat. Nanotechnol.* **2013**, *8*, 506.
- [16] N. E. Watkins, J. Guan, B. T. Dirroll, K. R. Williams, R. D. Schaller, T. W. Odom, *J. Phys. Chem. C* **2021**, *125*, 19874.
- [17] T. K. Hakala, H. T. Rekola, A. I. Väkeväinen, J.-P. Martikainen, M. Nečáda, A. J. Moilanen, P. Törmä, *Nat. Commun.* **2017**, *8*, 13687.
- [18] C. Deeb, Z. Guo, A. Yang, L. Huang, T. W. Odom, *Nano Lett.* **2018**, *18*, 1454.

- [19] Y. Xia, G. M. Whitesides, *Angew Chem Int Ed Engl* **1998**, *37*, 550.
- [20] J. Henzie, M. H. Lee, T. W. Odom, *Nat. Nanotechnol.* **2007**, *2*, 549.
- [21] D. Wang, W. Wang, M. P. Knudson, G. C. Schatz, T. W. Odom, *Chem. Rev.* **2018**, *118*, 2865.
- [22] D. Wang, M. R. Bourgeois, W.-K. Lee, R. Li, D. Trivedi, M. P. Knudson, W. Wang, G. C. Schatz, T. W. Odom, *Nano Lett.* **2018**, *18*, 4549.
- [23] J. Guan, L. K. Sagar, R. Li, D. Wang, G. Bappi, N. E. Watkins, M. R. Bourgeois, L. Levina, F. Fan, S. Hoogland, O. Voznyy, J. M. de Pina, R. D. Schaller, G. C. Schatz, E. H. Sargent, T. W. Odom, *Nano Lett.* **2020**, *20*, 1468.
- [24] J. Guan, L. K. Sagar, R. Li, D. Wang, G. Bappi, W. Wang, N. Watkins, M. R. Bourgeois, L. Levina, F. Fan, S. Hoogland, O. Voznyy, J. M. de Pina, R. D. Schaller, G. C. Schatz, E. H. Sargent, T. W. Odom, *ACS Nano* **2020**, *14*, 3426.
- [25] Y. Yin, Y. Lu, B. Gates, Y. Xia, *J. Am. Chem. Soc.* **2001**, *123*, 8718.
- [26] J. Yao, X. Yan, G. Lu, K. Zhang, X. Chen, L. Jiang, B. Yang, *Adv. Mater.* **2004**, *16*, 81.
- [27] J. A. Fan, K. Bao, L. Sun, J. Bao, V. N. Manoharan, P. Nordlander, F. Capasso, *Nano Lett.* **2012**, *12*, 5318.
- [28] C. Hanske, M. Tebbe, C. Kuttner, V. Bieber, V. V. Tsukruk, M. Chanana, T. A. F. König, A. Fery, *Nano Lett.* **2014**, *14*, 6863.
- [29] K. Volk, T. Honold, D. Feller, M. Karg, *Adv. Mater. Interfaces* **2021**, *8*, 2100317.
- [30] E. Ponomareva, K. Volk, P. Mulvaney, M. Karg, *Langmuir* **2020**, *36*, 13601.
- [31] K. Volk, J. P. S. Fitzgerald, M. Karg, *ACS Appl. Mater. Interfaces* **2019**, *11*, 16096.
- [32] H. Zhang, X. Bu, S. Yip, X. Liang, J. C. Ho, *Adv. Intell. Syst.* **2020**, *2*, 1900085.
- [33] N. Denkov, O. Velev, P. Kralchevski, I. Ivanov, H. Yoshimura, K. Nagayama, *Langmuir* **1992**, *8*, 3183.
- [34] Z. Cai, Z. Li, S. Ravaine, M. He, Y. Song, Y. Yin, H. Zheng, J. Teng, A. Zhang, *Chem. Soc. Rev.* **2021**, *50*, 5898.
- [35] N. Lassaline, R. Brechbühler, S. J. W. Vonk, K. Ridderbeek, M. Spieser, S. Bisig, B. le Feber, F. T. Rabouw, D. J. Norris, *Nature* **2020**, *582*, 506.
- [36] A. F. M. Leenaars, J. A. M. Huethorst, J. J. Van Oekel, *Langmuir* **1990**, *6*, 1701.
- [37] R. D. Deegan, O. Bakajin, T. F. Dupont, G. Huber, S. R. Nagel, T. A. Witten, *Nature* **1997**, *389*, 827.
- [38] L. Scarabelli, D. Vila-Liarte, A. Mihi, L. M. Liz-Marzán, *Acc Mater Res* **2021**, *2*, 816.
- [39] P. Molet, N. Passarelli, L. A. Pérez, L. Scarabelli, A. Mihi, *Adv. Opt. Mater.* **2021**, *9*, 2100761.
- [40] O. Colomer-Ferrer, S. T. Cosi, Y. Conti, D. E. Medina-Quiroz, L. Scarabelli, A. Mihi, *J. Mater. Chem. C* **2022**, *10*, 13913.
- [41] D. Wang, M. R. Bourgeois, J. Guan, A. K. Fumani, G. C. Schatz, T. W. Odom, *ACS Photonics* **2020**, *7*, 630.
- [42] A. J. C. Kuehne, M. C. Gather, *Chem. Rev.* **2016**, *116*, 12823.
- [43] M. N. Shkunov, Z. V. Vardeny, M. C. DeLong, R. C. Polson, A. A. Zakhidov, R. H. T. Baughman, *Adv. Funct. Mater.* **2002**, *12*, 21.
- [44] S.-H. Kim, S.-H. Kim, W. C. Jeong, S.-M. Yang, *Chem. Mater.* **2009**, *21*, 4993.
- [45] R. Guo, T. K. Hakala, P. Törmä, *Phys. Rev. B* **2017**, *95*, 155423.
- [46] V. Gupta, P. T. Probst, F. R. Goßler, A. M. Steiner, J. Schubert, Y. Brasse, T. A. F. König, A. Fery, *ACS Appl. Mater. Interfaces* **2019**, *11*, 28189.
- [47] E. S. A. Goerlitzer, R. Mohammadi, S. Nechayev, K. Volk, M. Rey, P. Banzer, M. Karg, N. Vogel, *Adv. Mater.* **2020**, *32*, 2001330.
- [48] S. A. Maier, *Plasmonics: Fundamentals and Applications*, Springer, New York, **2007**.
- [49] L. Zundel, P. Gieri, S. Sanders, A. Manjavacas, *Adv. Opt. Mater.* **2022**, *10*, 2102550.
- [50] C. Battocchio, C. Meneghini, I. Fratoddi, I. Venditti, M. V. Russo, G. Aquilanti, C. Maurizio, F. Bondino, R. Matassa, M. Rossi, S. Mobilio, G. Polzonetti, *J. Phys. Chem. C* **2012**, *116*, 19571.
- [51] A. H. Schokker, A. F. Koenderink, *Phys. Rev. B* **2014**, *90*, 155452.
- [52] B. F. E. Matarèse, P. L. C. Feyen, A. Falco, F. Benfenati, P. Lugli, J. C. deMello, *Sci. Rep.* **2018**, *8*, 5560.
- [53] C. Hanske, E. H. Hill, D. Vila-Liarte, G. González-Rubio, C. Matricardi, A. Mihi, L. M. Liz-Marzán, *ACS Appl. Mater. Interfaces* **2019**, *11*, 11763.
- [54] M. Anyfantakis, D. Baigl, *Chemphyschem* **2015**, *16*, 2726.
- [55] Z.-Z. Gu, A. Fujishima, O. Sato, *Angew. Chem., Int. Ed.* **2002**, *41*, 2067.
- [56] W. Cheng, N. Park, M. T. Walter, M. R. Hartman, D. Luo, *Nat. Nanotechnol.* **2008**, *3*, 682.
- [57] S. Sarkar, V. Gupta, M. Kumar, J. Schubert, P. T. Probst, J. Joseph, T. A. F. König, *ACS Appl. Mater. Interfaces* **2019**, *11*, 13752.
- [58] T. J. Palinski, B. E. Vyhnaek, G. W. Hunter, A. Tadimety, J. X. J. Zhang, *IEEE J. Sel. Top. Quantum Electron.* **2021**, *27*, 4600710.
- [59] J. Liu, B. Xu, J. Zhang, G. Song, *Plasmonics* **2013**, *8*, 995.
- [60] J. M. Winkler, M. J. Ruckriegel, H. Rojo, R. C. Keitel, E. De Leo, F. T. Rabouw, D. J. Norris, *ACS Nano* **2020**, *14*, 5223.
- [61] W. Wang, M. Ramezani, A. I. Väkeväinen, P. Törmä, J. G. Rivas, T. W. Odom, *Mater. Today* **2018**, *21*, 303.
- [62] M. Juodėnas, T. Tamulevičius, J. Henzie, D. Erts, S. Tamulevičius, *ACS Nano* **2019**, *13*, 9038.
- [63] A. Manjavacas, L. Zundel, S. Sanders, *ACS Nano* **2019**, *13*, 10682.
- [64] N. B. Tomazio, L. D. Boni, C. R. Mendonca, *Sci. Rep.* **2017**, *7*, 8559.
- [65] O. Svelto, *Introductory Concepts.*, In, *Principles of Lasers*, Ed.: O. Svelto, Springer US, Boston, MA, **2010**, pp 1–15. https://doi.org/10.1007/978-1-4419-1302-9_1.
- [66] I. D. W. Samuel, E. B. Namdas, G. A. Turnbull, *Nat. Photonics* **2009**, *3*, 546.
- [67] N. Passarelli, R. Bustos-Marún, R. Depine, *J. Phys. Chem. C* **2019**, *123*, 13015.
- [68] S.-H. Chang, A. Taflove, *Opt. Express* **2004**, *12*, 3827.
- [69] D. Khlopin, F. Laux, W. P. Wardley, J. Martin, G. A. Wurtz, J. Plain, N. Bonod, A. V. Zayats, W. Dickson, D. Gérard, *J Opt Soc Am B* **2017**, *34*, 691.
- [70] *Nat. Photonics* **2017**, *11*, 139.
- [71] S. Hamdad, A. T. Diallo, M. Chakaroun, A. Boudrioua, *Sci. Rep.* **2022**, *12*, 3218.
- [72] A. K. Boddeti, J. Guan, T. Sentz, X. Juarez, W. Newman, C. Cortes, T. W. Odom, Z. Jacob, *Nano Lett.* **2022**, *22*, 22.
- [73] V. G. Kravets, F. Schedin, A. V. Kabashin, A. N. Grigorenko, *Opt. Lett.* **2010**, *35*, 956.
- [74] D. F. Swearer, B. B. Bourgeois, D. K. Angell, J. A. Dionne, *Acc. Chem. Res.* **2021**, *54*, 3632.
- [75] M. Herran, A. Sousa-Castillo, C. Fan, S. Lee, W. Xie, M. Döblinger, B. Auguie, E. Cortés, *Adv. Funct. Mater.* **2020**, *30*, 2203418, 2203418.
- [76] J. Plou, I. García, M. Charconnet, I. Astobiza, C. García-Astrain, C. Matricardi, A. Mihi, A. Carracedo, L. M. Liz-Marzán, *Adv. Funct. Mater.* **2020**, *30*, 1910335.
- [77] J. Plou, M. Charconnet, I. García, J. Calvo, L. M. Liz-Marzán, *ACS Nano* **2021**, *15*, 8984.
- [78] E. Cortés, F. J. Wendisch, L. Sortino, A. Mancini, S. Ezendam, S. Saris, S. de L. Menezes, A. Tittl, H. Ren, S. A. Maier, *Chem. Rev.* **2022**, *15082*, <https://doi.org/10.1021/acs.chemrev.2c00078>.
- [79] I. Lee, D. Kim, J. Kal, H. Baek, D. Kwak, D. Go, E. Kim, C. Kang, J. Chung, Y. Jang, S. Ji, J. Joo, Y. Kang, *Adv. Mater.* **2010**, *22*, 4973.
- [80] N. G. Bastús, F. Merkoçi, J. Piella, V. Puntes, *Chem. Mater.* **2014**, *26*, 2836.
- [81] L. F. Paz, M. Caño-García, M. A. Geday, J. M. Otón, X. Quintana, *Sci. Rep.* **2022**, *12*, 6142.